


Cite this: *RSC Adv.*, 2017, 7, 19849

Magnetically recyclable self-assembled thin films for highly efficient water evaporation by interfacial solar heating†

Rong Chen, Zhejian Wu, Tuqiao Zhang, Tingchao Yu* and Miaomiao Ye *

Magnetic microspheres including Fe_3O_4 , MnFe_2O_4 , ZnFe_2O_4 , and CoFe_2O_4 have been synthesized via a simple solvothermal method followed by surface hydrophobization with 1H,1H,2H,2H-perfluorooctyltrichlorosilane. The hydrophobic magnetic microspheres can self-assemble into a thin film under simulated solar light irradiation and float on the surface of water. The formed film was used as photothermal material for water evaporation based on a new concept of interfacial solar heating. The water evaporation efficiency was significantly enhanced by the Fe_3O_4 thin film, and is about 1.4, 1.7 and 2.2 times higher than that without the formation of a Fe_3O_4 thin film, Fe_3O_4 uniformly dispersed in water, and water evaporation itself, respectively. The temperature gradient distributions from the surface to the bottom of the water directly demonstrated the advantage of interfacial solar heating for water evaporation. We believe that the water evaporation efficiency with the magnetic thin film is mainly due to the high light absorption, rapid heat transfer and good solid–liquid adhesion performance. In addition, the hydrophobic magnetic microspheres also have advantages over other reported photothermal materials due to their easy recycling, non-toxicity, low dose, and low cost.

Received 13th March 2017

Accepted 23rd March 2017

DOI: 10.1039/c7ra03007j

rsc.li/rsc-advances

Introduction

More and more people in the world, especially in the Middle East, Africa, and some island countries, are suffering from a shortage of fresh water because of climate change, population growth, water resource pollution, *etc.*^{1,2} Sea water desalination has been labeled as the main solution to the water shortage since it can offer abundant fresh water for drinking and for industry use.³ In practical applications, two mature processes are widely used for sea water desalination, which are reverse osmosis (RO) and multi-stage flash (MSF) distillation.⁴ However, both of these desalination processes consume a large quantity of electrical energy resulting in a high water charge and a large emission of greenhouse gases.⁵ Furthermore, the growth of marine organisms may be affected or they may even be killed during the seawater intake process and high salinity seawater discharge process.^{6,7} In addition, these two desalination processes cannot be carried out in some remote and rural areas

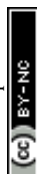
where electric power and centralized water desalination are still unavailable.

Recently, a new strategy named “Air–Water Interface Solar Heating” has been employed for seawater desalination.^{8,9} In this new desalination process, solar absorption materials float on the surface of seawater or brackish water, and only heat the water surface while avoiding uniformly heating the bulk water. Therefore, the evaporation efficiency will be significantly enhanced due to the high light-to-heat conversion rate. Up to now, solar absorption materials including Au nanoparticles, Al nanoparticles, carbon nanotubes, graphite, graphene, polypyrrole, *etc.*^{9–21} have been investigated for water evaporation based on the above new concept. However, photothermal materials are usually immobilized on some floating supporting materials, which results in a decrease of the surface-to-volume ratio and the inadequate utilization of these functional materials since part of the material surfaces is adhered to the supporting materials.²² In some cases, they may detach from the support since the immobilization is typically realized through physical adhesion. In addition, some of these solar adsorption materials are high-cost, toxic, and difficult to recycle. The dosage of the solar absorption materials used for solar evaporation is usually large or not given in some cases,^{8,20,23} which not only causes material wastage but also prevents comparison of solar evaporation efficiencies among reported solar absorption materials.

In this paper, we demonstrate the “Air–Water Interface Solar Heating” process for water evaporation using magnetic

Zhejiang Key Laboratory of Drinking Water Safety and Distribution Technology, Zhejiang University, Hangzhou, 310058, PR China. E-mail: yemiao008@zju.edu.cn; tingchaoyu@163.com; Tel: +86-571-88206759

† Electronic supplementary information (ESI) available: Spectrum of the xenon lamp; XRD, N_2 adsorption–desorption, and contact angles of MFe_2O_4 microspheres; XRD, and contact angles of Fe_3O_4 microspheres after 10 cycles; BET surface areas, total pore volume, average pore diameters, and proportion of light absorption of MFe_2O_4 microspheres; evaporation efficiencies of different water evaporation processes. See DOI: 10.1039/c7ra03007j



microspheres (Fe_3O_4 , MnFe_2O_4 , ZnFe_2O_4 , and CoFe_2O_4) as the solar adsorption materials. The magnetic microspheres were surface modified with 1H,1H,2H,2H-perfluorooctyltrichlorosilane (PFOTS) so that they could float on the surface of water. After that, a thin film was assembled during the simulated solar light irradiation. The formation of the thin film with a low Fe_3O_4 dose significantly enhanced the water evaporation efficiency. Furthermore, we also demonstrated the new concept of interfacial solar heating for water evaporation by measuring the temperature from the surface to the bottom of the water. Finally, the recycling properties and chemical stability of the hydrophobic magnetic microspheres were also investigated.

Experimental

Materials

Iron(III) chloride (FeCl_3 , 97%) and PFOTS (97%) were purchased from Sigma-Aldrich Co, USA. Manganese(II) chloride (MnCl_2 , >98%), zinc(II) chloride (ZnCl_2 , >98%), cobalt(II) chloride (CoCl_2 , >99%), anhydrous sodium acetate (NaAc , >99%), polyethylene glycol (PGE, >99%), ethylene glycol (EG, >99%), ethanol, and *n*-hexane (>99%) were purchased from Shanghai Chemical Reagent Co, China. All of the reagents used were of analytical grade and used without further purification.

Synthesis of Fe_3O_4 and MFe_2O_4 ($\text{M} = \text{Mn, Zn, Co}$) microspheres

The Fe_3O_4 and MFe_2O_4 ($\text{M} = \text{Mn, Zn, Co}$) microspheres were synthesized *via* a simple solvothermal process, which has been reported elsewhere.²⁴ Typically, to prepare the Fe_3O_4 microspheres, 0.811 g of FeCl_3 was firstly dissolved in 40 mL of ethylene glycol (GE) to form a transparent solution, then 3.6 g of NaAc and 1.0 g of polyethylene glycol (PEG) were added to the above transparent solution. The mixture was stirred vigorously for 2 h and then transferred to a 50 mL teflon-lined stainless-steel autoclave. The autoclave was heated at 200 °C for 8 h and then cooled to room temperature. The black products were collected and washed with ethanol three times. The MFe_2O_4 ($\text{M} = \text{Co, Mn, Zn}$) microspheres were synthesized by the coprecipitation of M(II) and Fe(III) chlorides (the molar ratio of $\text{M}^{2+}/\text{Fe}^{3+} = 0.5$). Typically, 0.811 g (5 mmol) of FeCl_3 and 0.315 g (2.5 mmol) of MnCl_2 were firstly dissolved in 40 mL of ethylene glycol to form a transparent solution, then the same synthesis process as for the preparation of the Fe_3O_4 microspheres was followed.

Hydrophobization of the magnetic microspheres

The as-prepared Fe_3O_4 and MFe_2O_4 ($\text{M} = \text{Mn, Zn, Co}$) magnetic microspheres were firstly washed with *n*-hexane 3 times, then transferred into 4 mL of *n*-hexane (containing 0.5% PFOTS). The mixture was sonicated for 20 min and dried in air at 60 °C for 4 h.

Characterization

The crystal structures of the samples were analyzed using a D/Max-RA X-ray diffractometer (Rigaku, Japan) with $\text{Cu K}\alpha$

radiation ($\lambda = 1.5418 \text{ \AA}$). The morphologies and sizes of the samples were examined by a transmission electron microscope (TEM, a JEOL JEM1200EX microscope at an accelerating voltage of 100 kV). The BET surface areas and pore size distributions of the samples were measured by a nitrogen adsorption-desorption experiment (Quantachrome, ASiC-2 measuring instrument). The ultraviolet-visible-near-infrared (UV-Vis-NIR) diffuse reflectance spectra of the samples were characterized using a UV-Vis-NIR spectrophotometer system (U-4100, Hitachi Japan), carrying out absolute hemispherical measurements. The reference was the reflection of the blank BaSO_4 sample. In order to test the hydrophobicity of the samples, small amounts of powder were pressed into a disc to measure the contact angle using an OCA20 contact angle measuring device (Dataphysics, Germany).

Water evaporation

Water evaporation experiments were carried out at a room temperature of $25 \pm 1 \text{ }^\circ\text{C}$ and at an air humidity of $\sim 60\%$. The magnetic powder floated on the surface of 200 mL of water in a 250 mL beaker. Before the experiment, the magnetic powder floating on the surface of water was irradiated under a 300 W xenon lamp for 4 h to form a thin film. The beaker was then placed on an electronic balance to measure the weight of the evaporated water. A 300 W xenon lamp (CEL-HXF300, 15A, Beijing Jin Yuan Science and Technology Co., China, the wavelength spectrum and intensity can be found in Fig. S1, ESI†) was used as a solar light simulator. The light source was vertically fixed to the surface of the water at a distance of 5.5 cm. The water temperatures from the surface to the bottom were measured using a Type K-thermocouple and recorder (YUWESE, SSN-61). The concentrations of dissolved Fe^{3+} in the water during the evaporation process were determined using a PerkinElmer NexION 350Q ICP-MS Spectrometer.

Results and discussion

Characterization of magnetic microspheres

The XRD patterns of the as-prepared samples are shown in Fig. S2, ESI†. All of the diffraction peaks can be readily indexed to the cubic spinel structure of Fe_3O_4 (JCPDS 75-1609), MnFe_2O_4 (JCPDS 74-2403), ZnFe_2O_4 (JCPDS 22-1012), and CoFe_2O_4 (JCPDS 22-1086). No characteristic peaks of other impurities were detected in the XRD patterns, indicating the high purity of all of the samples. The morphologies and sizes of the magnetic microspheres were characterized using a transmission electron microscope (TEM), and the results are shown in Fig. 1. The solvothermal method leads to the complete formation of solid spherical structures, and the average particle sizes of the Fe_3O_4 , MnFe_2O_4 , ZnFe_2O_4 and CoFe_2O_4 microspheres are about 480 nm, 285 nm, 320 nm, and 135 nm, respectively. The surface areas, pore volumes and pore size distributions of the magnetic microspheres were investigated using N_2 adsorption-desorption isotherms, the results are shown in Fig. S3, ESI†. The data concerning the BET surface areas, pore volumes and average



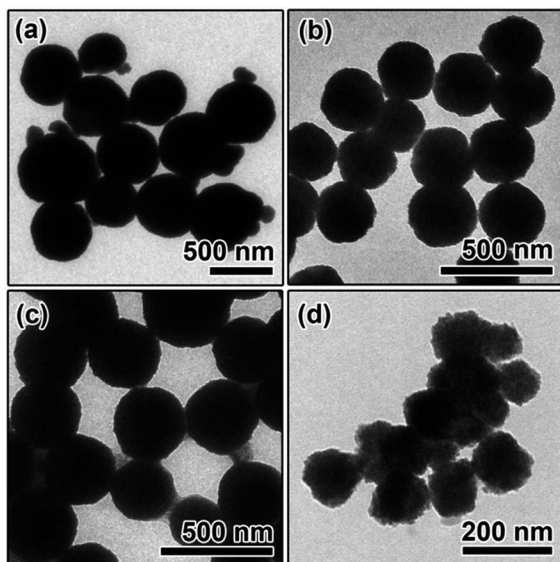


Fig. 1 TEM images of (a) Fe_3O_4 , (b) MnFe_2O_4 , (c) ZnFe_2O_4 , and (d) CoFe_2O_4 microspheres.

pore sizes of the different magnetic microspheres are presented in Table S1, ESI†

Fig. 2 shows the Ultraviolet-Visible-Near-Infrared (UV-Vis-NIR) absorption spectra of these four magnetic microspheres. For all of the samples, the photo-response from the ultraviolet (<400 nm) to the visible (400–760 nm) and near-infrared (760–2200 nm) spectral regions can be observed. Herein, the solar absorption of the Fe_3O_4 , MnFe_2O_4 , ZnFe_2O_4 and CoFe_2O_4 microspheres can be calculated using the following equation:²⁵

$$A = \frac{\int (1 - R) S d\lambda}{\int S d\lambda} \quad (1)$$

where A is the solar absorption, R is the reflectance of the sample, S is the solar spectral irradiance ($\text{W m}^{-2} \text{nm}^{-1}$), and λ is the wavelength (nm). Here, $(1 - R) \cdot S$ represents the sample absorption of solar spectral irradiance. The solar absorption of the Fe_3O_4 , MnFe_2O_4 , ZnFe_2O_4 and CoFe_2O_4 microspheres was

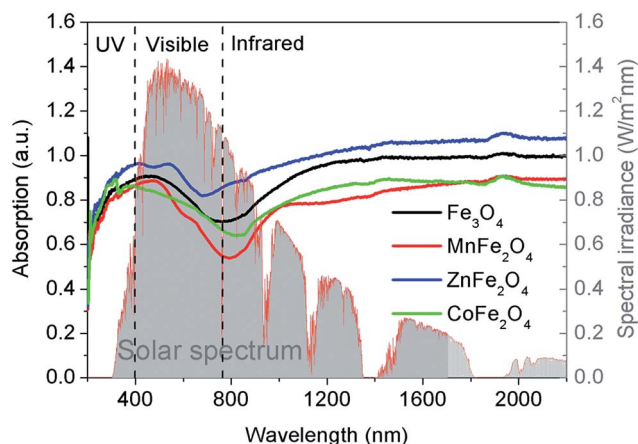


Fig. 2 Solar spectrum and UV-Vis-NIR absorption spectra of the magnetic microspheres.

therefore calculated to be 86.05%, 82.20%, 88.78%, and 83.68%, respectively. It has been reported that when the nanoparticles absorb solar energy, the energy is dissipated into the surrounding water, otherwise the particles will absorb heat and melt.¹⁷ In our case, almost none of the magnetic microspheres were dissolved in water during evaporation (which will be discussed later), indicating the high heat exchange between the water and the magnetic particles. The detailed solar absorptions in the ultraviolet to visible and infrared wavelength regions of all samples are displayed in Table S2, ESI†

To achieve the self-floating capability, the magnetic microspheres were modified by hydrophobization with PFOTS. To test the hydrophobic properties, the magnetic powder was pressed into a disc (the same as the KBr pellet pressing method). After the hydrophobic modification of Fe_3O_4 , it exhibited a high water contact angle of $\sim 146^\circ$ (as shown in Fig. 3a). Furthermore, the water droplet still firmly adhered to the surface when we rotated the disc with a tilt angle of 60° , 90° or 180° (see Fig. 3b–d), which indicates the high adhesion properties of the fluoroalkylsilane modified Fe_3O_4 microspheres. According to Wenzel's wetting behavior,^{26–28} the modified hydrophobic surface has a double wetting property, one is the high contact angle and the other is the high adhesion performance, which not only makes the material float on the surface of the water but also penetrates the surface of the material to achieve the maximum contact area and the maximum heat transfer. The water evaporation efficiency with the fluoroalkylsilane modified Fe_3O_4 microspheres will be enhanced due to Wenzel's wetting behavior. In addition, the water contact angles of MnFe_2O_4 , ZnFe_2O_4 and CoFe_2O_4 are 110° , 122° , and 120° (see Fig. S4, ESI†), respectively. Though the water contact angles are slightly less than that of Fe_3O_4 , the materials are also hydrophobic.

Water evaporation

For the application of the hydrophobic magnetic microspheres in water evaporation, the hydrophobic magnetic microspheres

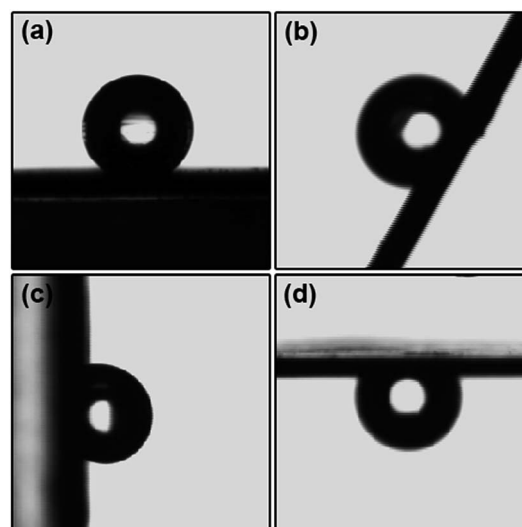


Fig. 3 The shapes of a water droplet on the Fe_3O_4 discs at different tilt angles of (a) 0° , (b) 60° , (c) 90° , and (d) 180° .



were first floated on the surface of water (see Fig. 4 top). After irradiation under a xenon lamp for 4 hours, a thin film was assembled with the assistance of the water molecules' thermal motion (see Fig. 4 bottom). The thickness of the thin film is composed of one or two Fe_3O_4 microspheres, therefore it can be calculated to be approximately 0.5–1.0 μm (see Fig. S5, ESI†). The formation of a thin film with magnetic microspheres will benefit light adsorption since the entire water surface is covered with this thin film. Therefore, the water evaporation efficiency will significantly increase due to the large area of the film, less aggregation of the particles, and the high-efficiency of the heat transfer. Fig. 5 shows the effect of the formation of the thin film on the water evaporation efficiency with the Fe_3O_4 microspheres. It can be clearly seen that the water evaporation efficiency with Fe_3O_4 with the formation of a thin film is significantly higher than that without the formation of a thin film. The water evaporation with the Fe_3O_4 microspheres with and without the formation of a thin film, and the Fe_3O_4 microspheres uniformly dispersed in the water, can be modeled by zero-order kinetics. The water evaporation reaction can be described simply by $m - m_0 = -kt$, where m and m_0 are the actual water mass at time t and initial water mass respectively, and k is the water evaporation efficiency. The zero-order kinetics equations and the water evaporation efficiency (k) of the different samples and processes are calculated in Table S3, ESI†. The water evaporation efficiency with the Fe_3O_4 thin film is about 1.4, 1.7, and 2.2 times higher than that without the formation of a thin film, Fe_3O_4 uniformly dispersed in water, and water itself, respectively. These results strongly prove the advantage of interfacial solar heating for water evaporation. We therefore conclude that the interfacial solar heating process for water evaporation is an efficient technique for future application in sea water or brackish water desalination.

Moreover, the water evaporation efficiencies with different dosages of the Fe_3O_4 microspheres floating on the water surface with and without the formation of a thin film were also investigated to double check the interfacial heating effect, and the results are shown in Fig. 6. Without the formation of a thin film, the water evaporation efficiencies obviously increased on

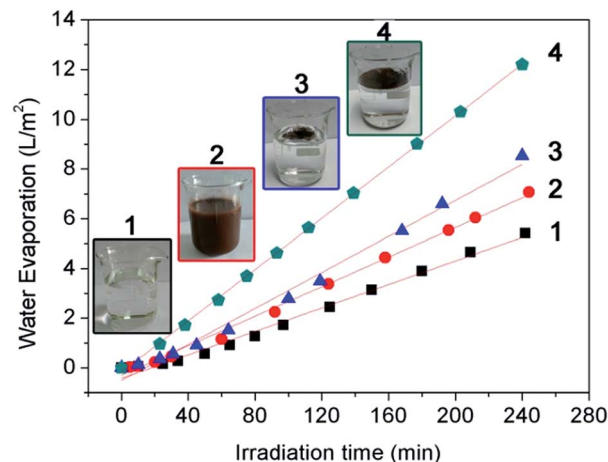


Fig. 5 Water evaporation performances with 150 mg of the Fe_3O_4 microspheres floating on the water surface with and without the formation of a thin film, 150 mg of Fe_3O_4 uniformly dispersed in the water, and water itself evaporating under solar light irradiation.

increasing the dosage of the Fe_3O_4 microspheres. This is because the increased dosage of the Fe_3O_4 microspheres led to the larger light-adsorption area on the water surface (as shown in the top of Fig. 4). However, with the formation of a thin film, the water evaporation efficiencies remained almost unchanged on increasing the dosage of Fe_3O_4 . This is because the addition of 50 mg of the Fe_3O_4 microspheres is enough for the formation a thin film with an area of 39.59 cm^2 (the same as the area of the beaker mouth) on the surface of the water. Further increasing the addition of the Fe_3O_4 microspheres just leads to the overlap and aggregation of the surface. The water evaporation efficiencies with different dosages ranging from 50 mg to 600 mg of the Fe_3O_4 microspheres floating on the water surface with the formation of thin films are 0.05079, 0.05159, 0.05388, and 0.05731 $\text{L m}^{-2} \text{min}^{-1}$, which are 1.6, 1.4, 1.3, and 1.1 times correspondingly higher than those without the formation of the thin films.

The high-efficiency heat transfer by interfacial solar heating was directly proven by measuring the temperature change during the water evaporation process. Fig. 7a shows the temperature change at the distance of 1.5 cm from the water surface in different evaporation processes (including water evaporation by Fe_3O_4 floating on the water surface with the

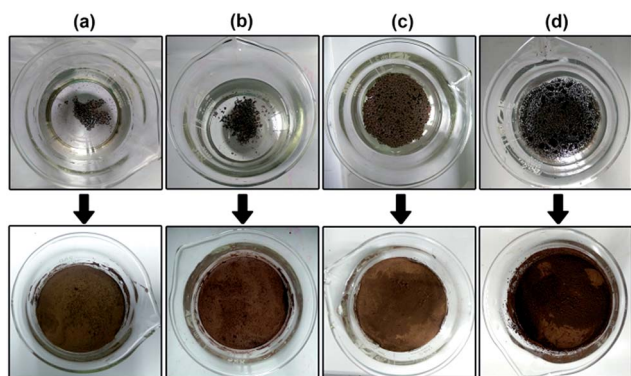


Fig. 4 Digital photos of (a) 50 mg (0.25 g L^{-1}), (b) 150 mg (0.75 g L^{-1}), (c) 300 mg (1.5 g L^{-1}), and (d) 600 mg (3.0 g L^{-1}) of the Fe_3O_4 microspheres floating on the water surface (bottom) with and (top) without formation of a thin film.

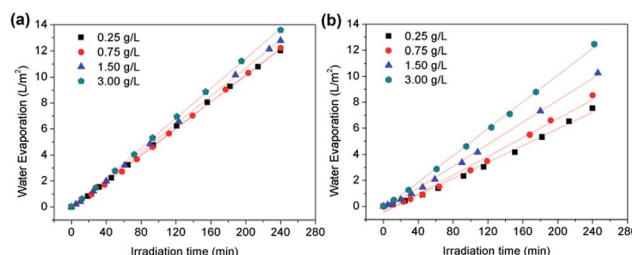


Fig. 6 Water evaporation performances with different dosages of the Fe_3O_4 microspheres floating on the water surface (a) with and (b) without the formation of a thin film.

formation of a thin film, Fe_3O_4 uniformly dispersed in the water, and water evaporating itself). It can be obviously seen that the temperature in the process of Fe_3O_4 floating on the water surface with the formation of a thin film possesses the fastest heating rate. The temperature rises up to 55.5°C at the evaporation time of 2 h, which is 5.7°C higher than that of the Fe_3O_4 microspheres uniformly dispersed in the water. In addition, to further confirm the interfacial heating effect, we vertically moved a temperature probe from the surface to the bottom of the water to measure the temperature change during the water evaporation process. Fig. 7b clearly displays the temperature distributions during water evaporation by the Fe_3O_4 microspheres floating on the water surface with the formation of a thin film. At the same irradiation time, the temperature increased with the decreasing distance from the water surface. For example, at the irradiation time of 2 h, the temperatures at the distances from the water surface of 0.7 cm, 1.5 cm, 2.0 cm, 4.0 cm, and 6.5 cm (bottom) are 66.3°C , 55.5°C , 47.1°C , 40.1°C and 40.0°C , respectively, which strongly confirms the interfacial heating effect of only heating the water surface while avoiding the uniform heating of the bulk water.

To confirm the photothermal effect of the other three types of hydrophobic MFe_2O_4 ($\text{M} = \text{Mn}, \text{Zn}, \text{Co}$) microspheres, the water evaporation experiments were carried out with the

addition of MFe_2O_4 ($\text{M} = \text{Mn}, \text{Zn}, \text{Co}$) with a dosage of 150 mg (0.75 g L^{-1}), and the results are shown in Fig. 8. The zero-order kinetics equations and evaporation efficiencies are also displayed in Table S3, ESI†. The water evaporation efficiency follows the order of $\text{MnFe}_2\text{O}_4 < \text{ZnFe}_2\text{O}_4 < \text{CoFe}_2\text{O}_4 < \text{Fe}_3\text{O}_4$. Generally, the water evaporation efficiency can be influenced by the light adsorption capacity, porosity, water contact angle, and adhesion effect of the magnetic microspheres. Here, the Fe_3O_4 microspheres possess the best water evaporation efficiency due to their big water contact angle, good adhesion effect and good light adsorption capacity. By contrast, the MnFe_2O_4 microspheres possess the worst water evaporation efficiency because they have the smallest water contact angle and the worst light adsorption capacity.

Cycling

Magnetic particles have advantages over other solar adsorption materials due to their convenient separation and recycling in liquid-phase reactions by applying external magnetic fields.²⁹ Herein, we demonstrate the quick separation of the Fe_3O_4 microspheres using a $46 \text{ mm} \times 46 \text{ mm} \times 22 \text{ mm}$ cuboid NdFeB magnet (as shown in Fig. 9a and b), in which the magnetic particles can be completely separated from the water surface within 10 seconds. To exploit the stability of the hydrophobic magnetic microspheres, the water evaporation efficiencies were monitored for ten cycles. A very slightly decreased water evaporation efficiency can be observed after ten cycles (as shown in Fig. 9c). Furthermore, the Fe_3O_4 microspheres still have a large water contact angle of 140° (see Fig. S6, ESI†) with the crystal structure unchanged (see Fig. S7, ESI†) after 10 cycles, which also confirms the high stability of the hydrophobic Fe_3O_4 microspheres. In addition, we also studied the chemical stability of the Fe_3O_4 microspheres by measuring the dissolved Fe^{3+} during the water evaporation process. The concentration of Fe^{3+} in the water was measured to be 0.37 mg L^{-1} (0.0248% of Fe_3O_4) in the first run, and gradually decreased to 0.11 mg L^{-1}

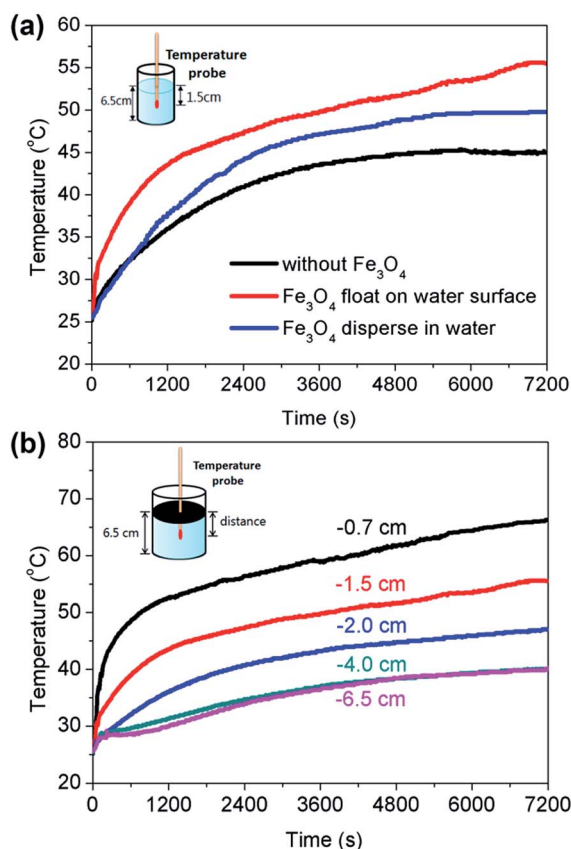


Fig. 7 (a) The temperature change at the distance of 1.5 cm from the water surface in different evaporation processes; (b) the temperature distributions during water evaporation by the Fe_3O_4 microspheres floating on the water surface with the formation of a thin film.

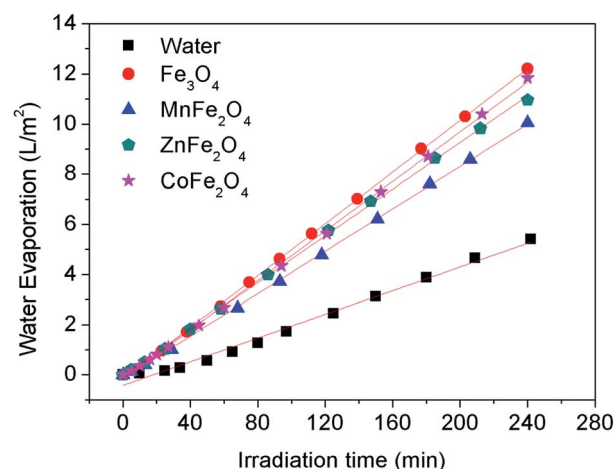


Fig. 8 Water evaporation performance with different hydrophobic magnetic microspheres floating on the water surface with the formation of a thin film.



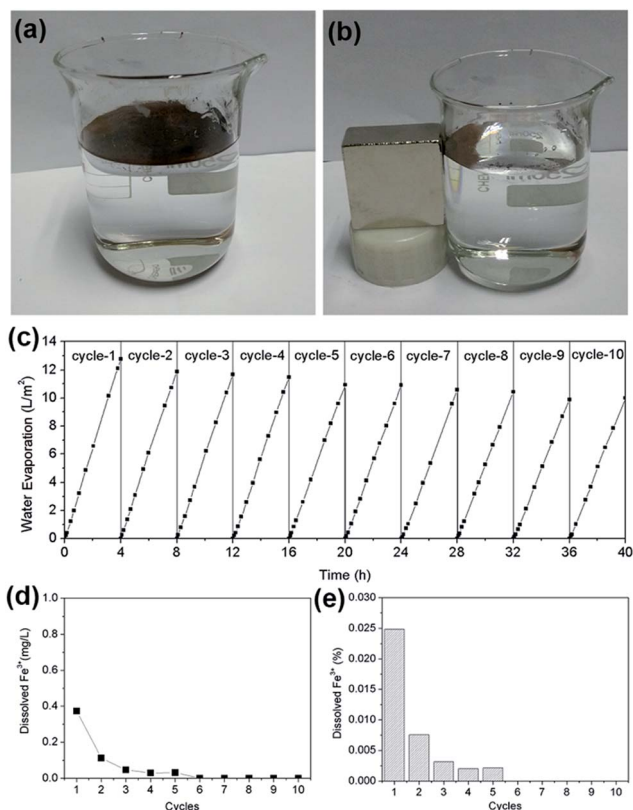


Fig. 9 (a and b) Separation process of hydrophobic Fe_3O_4 microspheres. (c) 10 cycles of water evaporation with hydrophobic Fe_3O_4 microspheres. (d) The concentration and (e) the proportion of the dissolved Fe^{3+} after different cycles of water evaporation.

(0.0075% of Fe_3O_4) in the fifth run. After 6 cycles, no Fe^{3+} could be detected. Firstly, we want to point out that the solar heating process is used to harvest fresh water, and the released ferric ions cannot be evaporated to the fresh water. Secondly, according to the Surface Water Quality Criteria set by the US Environmental Protection Agency (EPA), the concentration of iron for Class I is $\leq 1.0 \text{ mg L}^{-1}$, which means that the maximum concentration of the released ferric ions in the reaction solution still satisfies the Surface Water Quality Criteria. The concentration of the released ferric ions in the condensed water is 0.024 mg L^{-1} , which also satisfies the Surface Water Quality Criteria. Furthermore, PFOTS is a stable chemical, which cannot be decomposed completely by advanced oxidation processes (AOPs) such as UV irradiation, ozonation, TiO_2 -based photocatalysis, the persulfate oxidation process, etc.^{30–32} Our previous study also demonstrated that PFOTS cannot be decomposed under simulated sunlight irradiation with the light intensity of $\sim 1000 \text{ W m}^{-2}$ for 4 days.³³ These measurements demonstrated the high chemical stability of the hydrophobic Fe_3O_4 microspheres during the water evaporation process.

Conclusions

In summary, surface hydrophobized magnetic microspheres including Fe_3O_4 , MnFe_2O_4 , ZnFe_2O_4 , and CoFe_2O_4 were used for

water evaporation based on the new concept of interfacial solar heating. The self-assembly of a thin Fe_3O_4 film on the water surface significantly enhanced the water evaporation efficiency, which is 1.4, 1.7 and 2.2 times higher than that without the formation of a thin film, Fe_3O_4 uniformly dispersed in the water, and water itself evaporated under simulated solar light, respectively. The temperature distributions from the surface to the bottom of the water directly and strongly confirmed the interfacial heating effect. The enhanced water evaporation efficiency is mainly due to the high light-absorption capacity, rapid heat-transfer property and good solid-liquid adhesion performance. In addition, the magnetic microspheres have advantages over other reported photothermal materials due to their easy recycling, non-toxicity, good chemical stability, low dose, and low cost. Therefore, we believe our present work will offer a new approach to use photothermal materials for solar sea water or brackish water desalination.

Acknowledgements

This work was financially supported by the National Natural Science Foundation of China (No. 51108406), and the Important National Science and Technology Specific Projects (2012ZX07408-002, 2012ZX07403-004).

Notes and references

- W. Barnaby, *Nature*, 2009, **458**, 282–283.
- M. A. Montgomery and M. Elimelech, *Environ. Sci. Technol.*, 2007, **41**, 17–24.
- M. A. Shannon, P. W. Bohn, M. Elimelech, J. G. Georgiadis, B. J. Marinas and A. M. Mayes, *Nature*, 2008, **452**, 301–310.
- A. D. Khawaji, I. K. Kutubkhanah and J.-M. Wie, *Desalination*, 2008, **221**, 47–69.
- R. Semiat, *Environ. Sci. Technol.*, 2008, **42**, 8193–8201.
- S. Lattemann and T. Höpner, *Desalination*, 2008, **220**, 1–15.
- N. Ahmad and R. E. Baddour, *Ocean Coast Manag.*, 2014, **87**, 1–7.
- Y. Zeng, J. Yao, B. A. Horri, K. Wang, Y. Wu, D. Li and H. Wang, *Energy Environ. Sci.*, 2011, **4**, 4074–4078.
- L. Zhang, B. Tang, J. Wu, R. Li and P. Wang, *Adv. Mater.*, 2015, **27**, 4889–4894.
- K. Bae, G. Kang, S. K. Cho, W. Park, K. Kim and W. J. Padilla, *Nat. Commun.*, 2015, **6**, 10103.
- L. Zhou, Y. Tan, J. Wang, W. Xu, Y. Yuan, W. Cai, S. Zhu and J. Zhu, *Nat. Photonics*, 2016, **10**, 393–398.
- Y. Ito, Y. Tanabe, J. Han, T. Fujita, K. Tanigaki and M. Chen, *Adv. Mater.*, 2015, **27**, 4302–4307.
- Y. Liu, J. Chen, D. Guo, M. Cao and L. Jiang, *ACS Appl. Mater. Interfaces*, 2015, **7**, 13645–13652.
- Y. Liu, S. Yu, R. Feng, A. Bernard, Y. Liu, Y. Zhang, H. Duan, W. Shang, P. Tao and C. Song, *Adv. Mater.*, 2015, **27**, 2768–2774.
- J. Lou, Y. Liu, Z. Wang, D. Zhao, C. Song, J. Wu, N. P. Dasgupta, W. Zhang, D. Zhang and P. Tao, *ACS Appl. Mater. Interfaces*, 2016, **8**, 14628–14636.



- 16 O. Neumann, C. Feronti, A. D. Neumann, A. Dong, K. Schell, B. Lu, E. Kim, M. Quinn, S. Thompson and N. Grady, *Proc. Natl. Acad. Sci. U. S. A.*, 2013, **110**, 11677–11681.
- 17 O. Neumann, A. S. Urban, J. Day, S. Lal, P. Nordlander and N. J. Halas, *ACS Nano*, 2012, **7**, 42–49.
- 18 X. Wang, G. Ou, N. Wang and H. Wu, *ACS Appl. Mater. Interfaces*, 2016, **8**, 9194–9199.
- 19 Y. Wang, L. Zhang and P. Wang, *ACS Sustainable Chem. Eng.*, 2016, **4**, 1223–1230.
- 20 Y. Zeng, K. Wang, J. Yao and H. Wang, *Chem. Eng. Sci.*, 2014, **116**, 704–709.
- 21 H. Ghasemi, G. Ni, A. M. Marconnet, J. Loomis, S. Yerci, N. Miljkovic and G. Chen, *Nat. Commun.*, 2014, **5**, 4449.
- 22 A. Haarstrick, O. M. Kut and E. Heinzle, *Environ. Sci. Technol.*, 1996, **30**, 817–824.
- 23 Z. Wang, Y. Liu, P. Tao, Q. Shen, N. Yi, F. Zhang, Q. Liu, C. Song, D. Zhang and W. Shang, *Small*, 2014, **10**, 3234–3239.
- 24 H. Deng, X. Li, Q. Peng, X. Wang, J. Chen and Y. Li, *Angew. Chem., Int. Ed.*, 2005, **44**, 2782–2785.
- 25 T. Lin, C. Yang, Z. Wang, H. Yin, X. Lü, F. Huang, J. Lin, X. Xie and M. Jiang, *Energy Environ. Sci.*, 2014, **7**, 967–972.
- 26 R. N. Wenzel, *Ind. Eng. Chem.*, 1936, **28**, 988–994.
- 27 S. Wang and L. Jiang, *Adv. Mater.*, 2007, **19**, 3423–3424.
- 28 L. B. Zhang, J. B. Wu, M. N. Hedhili, X. L. Yang and P. Wang, *J. Mater. Chem. A*, 2015, **3**, 2844–2852.
- 29 M. Ye, Q. Zhang, Y. Hu, J. Ge, Z. Lu, L. He, Z. Chen and Y. Yin, *Chem.–Eur. J.*, 2010, **16**, 6243–6250.
- 30 M. F. Rahman, S. Peldszus and W. B. Anderson, *Water Res.*, 2014, **50**, 318–340.
- 31 O. Quinones and S. A. Snyder, *Environ. Sci. Technol.*, 2009, **43**, 9089–9095.
- 32 M. Chen, S. Lo, Y. Lee, J. Kuo and C. Wu, *J. Hazard. Mater.*, 2016, **303**, 111–118.
- 33 M. Ye, J. Jia, Z. Wu, C. Qian, R. Chen, P. G. O'Brien, W. Sun, Y. Dong and G. A. Ozin, *Adv. Energy Mater.*, 2017, **7**, 1601811.

